The effect of photonic crystal fibre structure on the performance of Mach-Zehnder interferometer fibre optic gas sensors

Kaveh Nazeri & Colin Bradley

June 2020

This article was originally published at:
https://doi.org/10.1016/j.yofte.2020.102294

Citation for this paper:

Nazeri, K., & Bradley, C. (2020). The effect of photonic crystal fibre structure on the performance of Mach-Zehnder interferometer fibre optic gas sensors. *Optical Fiber Technology*, 58, 1-10. https://doi.org/10.1016/j.yofte.2020.102294.

Optical Fiber Technology 58 (2020) 102294

Contents lists available at ScienceDirect

Optical Fiber Technology

journal homepage: www.elsevier.com/locate/yofte

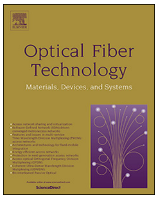

The effect of photonic crystal fibre structure on the performance of Mach-Zehnder interferometer fibre optic gas sensors

Kaveh Nazeri, Colin Bradley*

Department of Mechanical Engineering, University of Victoria, Victoria, BC V8P 5C2, Canada

ARTICLE INFO

Keywords:
Mach-Zehnder interferometer
Refractive index sensor
Gas sensor
Photonic crystal fiber
Hollow-core PCF

ABSTRACT

A compact refractive index (RI) sensor, based on the Mach-Zehnder Interferometer (MZI), has been developed and experimentally evaluated for the highly sensitive detection and quantification of gases (Helium, Methane, and Carbon Dioxide). The RI sensor utilizes a variety of fibre types: Single Mode Fibre (SMF), Photonic Crystal Fibre (PCF), and Hollow-Core Photonic Crystal Fibre (HC-PCF). In order to fabricate the MZI sensors, a short length of sensing fibre was positioned between a lead-in and a lead-out single mode fibre (SMF) with an air gap at each interface. Three types of sensors were fabricated using this configuration employing 4 mm stub of: (i) PCF, (ii) 10 µm HC-PCF, and (iii) 20 µm HC-PCF as the sensing elements. The performance of these sensors, for detecting and measuring the quantity of gas present, were compared. The transmission spectrum of MZI sensors are formed by interference between the cladding and core modes. These transmission signals correspond to the frequency components in the sensor's Fast Fourier Transform (FFT) spectrum. The effect of gap distance on the number and amplitude distribution of the modes was examined in an effort to optimize the design elements. The resulting fiber sensors can measure the RI of a gas-filled cavity and they showed high-sensitivity to helium, methane, and carbon dioxide. The highest RI sensitivity of 3210 nm/RIU was demonstrated in the RI range of 1.0000347-to-1.000449 by a sensor with a 4 mm long sensing stub element of 10 µm HC-PCF. Cyclic tests with the group of gases demonstrated that the measurements are highly repeatable. The measurement response and recovery times for all sensors were determined, and it was concluded that the 20 µm HC-PCF sensor has the fastest response/recovery time and the PCF sensor has the slowest. This research illustrates that the sensors fabricated by the proposed method have potential for improving the ability to detect and quantify pure gases. Additionally, the sensors are highly sensitive to low percentages of CO_2, making them suitable for greenhouse gas measurement.

1. Introduction

Properties of fiber optic sensors make them a superior choice for environmental monitoring applications, particularly when compared against conventional electro-optical sensors [1,2]. Their advantageous properties include multifunctional sensing capabilities (such as temperature, pressure, strain, and corrosion), immunity to electromagnetic radiation, and high sensitivity [1,3,4]. Sensing mechanisms such as evanescent field absorption, direct absorption, surface Plasmon resonance, and Raman scattering are among numerous fabrication methods that have been studied [5–10]. Resulting sensors have relied on different types of optical fibers, such as single mode fiber (SMF), photonic crystal fiber (PCF), and micro-structured fibers. Moreover, micro and nanostructured materials have been widely used to measure chemical entities, mostly by deposition of a material or polymer that is sensitive to a specific parameter on the fibre [11]. Thus, the light guidance is altered by changes in its optical properties. Several applications for detection of volatile organic compounds [12], gas sensing [13], and pH measuring [14] have been reported using this method. Nanostructured polymeric coatings such as nanoparticles, luminescent materials and metal oxide particles can enhance chemical, physical or optical properties of fibers in comparison with bulk material fibers [15]. It is been reported that implementation of sensitive coatings onto optical fibers can enhance some characteristics of a sensor like sensitivity and selectivity [15].

In addition to silica optical fibers, polymer optical fibers (POF) are well in use for fabrication of sensors in several sensing applications like strain [16], curvature [17], humidity [18], and temperature [19]. Advantages of POFs over silica fiber include higher flexibility in bending, higher fracture toughness [20], and higher thermo-optic coefficient

---

* Corresponding author.
E-mail addresses: nazerik@uvic.ca (K. Nazeri), cbr@uvic.ca (C. Bradley).

https://doi.org/10.1016/j.yofte.2020.102294
Received 29 April 2020; Received in revised form 2 June 2020; Accepted 4 June 2020

[21]. It should be noted that POF materials are viscoelastic, which lead to non-uniform results to strain or stress [22]. Various sensors have been developed and studied using POF, including Fiber Bragg Grating (FBG) inscription in POFs [20,22–24], and Long Period Gratings in microstructured POFs [25,26]. High stability, as well as minor variations in bandwidth and reflectivity are among the advantages of these sensors [20]. In the area of gas sensing, Saharudin et al. [27] used different oxygen sensitive nanomaterial to coat one end of optical fiber to evaluate the performance of sensors. Evaluation of the effect of sol–gel coated length on POF core is described by Zolkapli et al. [28] to improve oxygen gas sensitivity.

Further to previously mentioned methods, numerous types of optical fiber interferometers have been studied, including the Sagnac, Michelson, extrinsic/intrinsic Fabry-Perot, and Mach-Zehnder interferometers. Domingues et al. [29] developed an intrinsic Fabry-Perot interferometer (FP) micro-cavity for pressure sensing. They achieved the sensitivity of 59.39 ± 1.7 pm/Kpa for pressures up to 900 kPa, using a FP interferometer with micro-cavity length of 21.86 μm. As the cavity's physical parameters can induce phase shift on the FP interferometer signal, these sensors can be used to monitor pressure, temperature, strain, and refractive index. The hybrid FP engineered by R. Wang [30] simultaneously monitors RI change and temperature fluctuations, but has relatively low sensitivity in the RI range of 1.005–1.00275. A hybrid interferometer was proposed by Sun et al. [31] by forming a Fabry-Perot cavity in one of the optical paths of a Michelson interferometer. Consequently, two distinctive interference fringes on the spectral response were formed. The simultaneous measurement of temperature and RI revealed temperature sensitivity of 13 pm//°C and resolution of 8.7 E^{-4} in the RI range of 1.33 – 1.38. Jia et al. [32] developed a temperature compensated FP sensor for humidity monitoring and gas concentration analysis, using a hollow silica tube (HST) with inner diameter of 5 μm. Liu et al. [33] developed a photonic crystal fiber Sagnac interferometer by filling the central holes of the fiber with microfluidic analytes. Although high sensitivity and resolution was achieved, but filling the air holes of fiber is complicated. Among different types of interferometers, MZIs have received significant attention, because they are robust, compact, and have high levels of precision [34].

A typical fibre-optic MZI sensor configuration has a sensing arm and a reference arm as well as a splitter that divides incident light into these arms. Light propagating in the two resulting paths is recombined by a coupler. The sensors developed in this research field have employed techniques such as mismatch splicing [35], cladding collapse [36], and hollow-core fiber splicing [37]. The configuration of in-line MZI sensors is composed of two contact arms within the fiber formed by using different optical fibres. This includes long-period gratings (LPGs), microfibers, and tapered fibers [38–42]. The configuration of a PCF-MZI sensor can be similar to an in-line MZI sensor. By splicing a piece of PCF between two SMFs, collapsed regions are inevitably formed at both ends of the PCF. These regions play the role of splitter or coupler [43]. PCFs have solid core and periodically spaced air holes in the cladding. This provides them with unique properties of high transmission [44], low background noise [45], and tailored dispersion [46]. Hollow-Core PCF (HC-PCF) has a hollow core surrounded by a cladding that also contains air holes. The fundamental mode in HC-PCF has a quasi-Gaussian intensity distribution [47]. Air holes in the fibre enable gas sensing, as it provides the interaction between the propagated light and the gas molecules in the sensing region.

Using HC-PCF as an apparatus for gas detection was proposed in 1999 and many optical devices have subsequently been fabricated [48]. Such gas sensors were fabricated either by splicing HC-PCF to another fiber such as SMF, or without splicing using a variety of fiber connectors [49]. Fusion splicing of HC-PCF to SMF is more difficult to produce than splicing PCF to SMF, because of the presence of a hollow-core, which contains a much larger volume of air that tends to expand during splicing, thereby distorting the fibre structure. Butt coupling in opposite is a method to fabricate PCF-MZI sensors without splicing, in which a gap is created between the lead-in, sensing element, and lead-out fibers. The length of this gap can be controlled in the assembly process and the gap allows light coupling between the SMF and PCF elements. Due to the mode field diameter (MFD) mismatch between SMF and HC-PCF, the propagation of SMF fundamental mode into the hollow-core fiber will excite the fundamental mode and weaker higher order modes [49]. As it may takes time for gas molecules to fully permeate the HCF-PCF cavities, the fabrication of micro-channels on the cladding of the HC-PCF, employing either femtosecond laser or Focused Ion Beam machining, has been suggested as a means to accelerate the gas diffusion [50–52].

In this study, which is a continuation of a recent article by Nazeri et Al. [53], an in-line fiber-optic MZI sensor, using both PCF and HC-PCF fibres, is presented. The working principle of the sensor and the method of light propagation inside the gap-based gas sensor are discussed below. Important performance parameters for three types of fiber-optic MZI sensors are presented: namely, their RI sensitivities, response and recovery times, as well as the number and power distribution of modes. Relative RI detection was employed in this work due to difficulty in achieving high accuracy RI measurements in absolute RI detection [54]. The experimental results of the sensors' RI sensitivity to helium, methane, carbon dioxide, and argon are presented. Nitrogen (99.99% purity, at 18 Psi) with an RI of 1.0002944 was employed as the control reference for RI characterization. The sensors showed great repeatability in their sensitivities. Moreover, given the complications of ambient RI measurement, the effect of temperature cross-sensitivity has been addressed, due to the fact that the RI of most gases is a function of temperature.

2. Working principle

Fig. 1a presents a schematic illustration of the proposed sensor configuration. In this arrangement, a short piece of sensing element fiber (4 mm) was placed between two SMFs with gaps at both ends. The incoming single mode light wave enters through the lead-in SMF. Upon reaching the first sensor gap, it radiates from the SMF core, illuminating the solid/hollow-core and the cladding air holes of the sensing element. The SMF core acts as a pseudo-point light source, and the rapidly diverging beam excites the fundamental mode and higher order modes propagating in the circular channels of the sensing element. Interaction between the propagating light and the gas molecules takes place along the length of the sensing element fiber. Optical interference occurs at the second gap due to the phase difference between the fundamental and higher order modes. The SMF, positioned at the transmission end of the sensor, then transfers the interference spectrum to the spectrum analyzer. The device's reference and sensing arms are both in contact with gas molecules; however, the effect of RI change on the interference in the sensing arm is higher than in the reference arm. That imbalance occurs due to differences in optical-path lengths between the arms. The central solid-core of the PCF and hollow-core of HC-PCF act as the reference arm of the MZI, and the cladding air channels act as its sensing arms. The light guiding mechanisms in photonic crystal fibers are different from the total internal reflection phenomenon that occurs in typical fibers [55]. Generally, photonic crystal fibres support several higher order core modes and sometimes additional surface modes that are located on the core-cladding boundary [47]. HC-PCF provides a remarkably strong interaction between light particles and gas molecules, due to high optical field confinement [56]. Fig. 1b shows a schematic diagram of the light transmission, Optical Path Length (OPL) differences, and theoretical phase shifts in an MZI with a 4 mm long, 10 μm HC-PCF stub as the sensing element and 1 mm gap at each end. Theoretical phase shifts are calculated using equation (2).

The fiber-optic MZI sensor's interference spectrum depends on the difference in optical path length between the light propagating in the sensing arm and in the reference arm. The interference between core

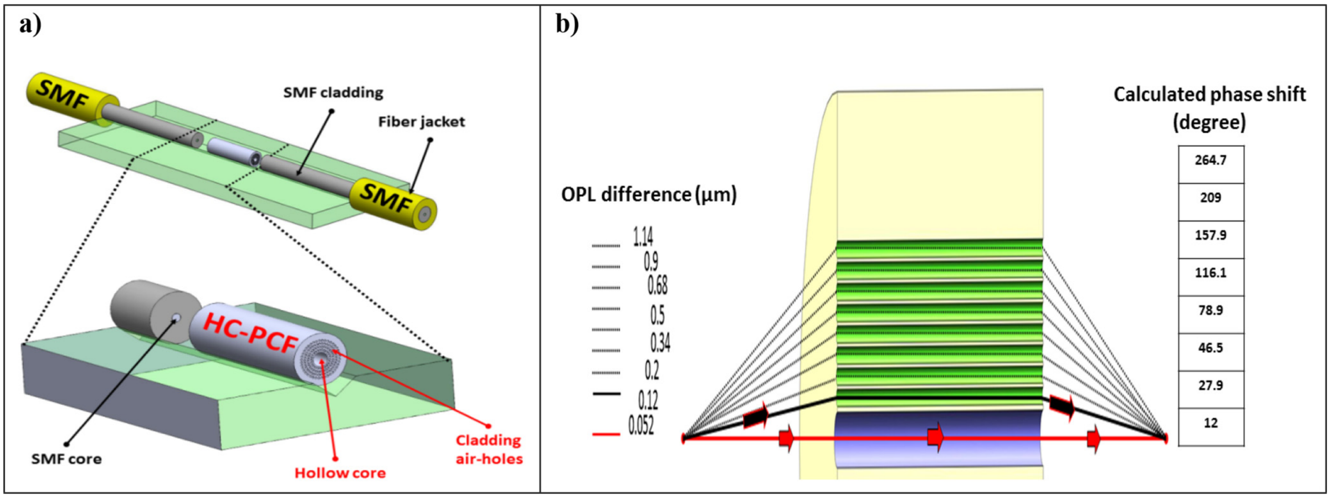

Fig. 1. (a) Schematic illustration of the proposed sensor arrangement, (b) Schematic of light transmission and OPL differences for an MZI with 4 mm length of 10 μm HC-PCF as sensing element, and gap length of 1 mm at each end.

and cladding modes can be written as a function of the phase difference (ϕ), core intensity (I_{core}), and cladding intensity ($I_{cladding}$) [34,53,57] as:

$$I = I_{core} + I_{cladding} + 2\sqrt{I_{core}I_{cladding}}\cos\varnothing \tag{1}$$

The phase difference ($\Delta\phi$) between the two modes traveling the same distance (L) can be written as:

$$\Delta\phi = 2\pi(\Delta n_{eff})L\lambda^{-1} \tag{2}$$

where λ is the input wavelength, Δn_{eff} is the difference in the effective RI between the core and cladding modes, and L is the path length of the sensing element fiber. Considering m as an integer, maximum transmission happens when $\Delta\Phi = 2\pi m$ and peaks at the following wavelength on the transmission signal:

$$\lambda_m = (\Delta n_{eff})Lm^{-1} \tag{3}$$

Consequently, the m-order shift of the interference spectrum is given by the following form:

$$\Delta\lambda_m = (\Delta n_{eff} + \Delta n)Lm^{-1} - \Delta n_{eff}m^{-1} = \Delta nLm^{-1} \tag{4}$$

Since the length of the PCF/HC-PCF (L) is constant in Eq. (4), then any change in the RI of core and cladding of the MZI will change Δn, and correspondingly $\Delta\lambda_m$. As a result, a change will occur in the outgoing spectrum due to optical interference, which depends on the OPL difference of light in the MZI's reference and sensing arms.

3. Sensor fabrication

The first step in the fabrication of fiber-optic MZI sensors consisted of using a femto-second laser to micro-machine a V-groove, having a width of 90 μm and depth of 50 μm, along a 25-mm-long microscope slide. The sensors were constructed on the slide, and the groove was used to position and align the lead-in SMF, lead-out SMF and sensing element fibre. The sensing element fibres include 4 mm of either PCF or HC-PCFs, and flat surfaces were cleaved onto both ends of the fiber sensing element. Their exact length was ensured by verification under an optical tooling microscope. The sensing element was then positioned in the middle of the lasered V-groove and fixed on the microscope slide using epoxy glue. Subsequently, the lead-in and lead-out SMFs were positioned in fibre holders, mounted on linear-translation stages, and were then aligned with the sensing element fibre and the V-groove. A top view of the fabrication setup is shown in Fig. 2a. Gap distances were accurately adjusted to control mode splitting/recombination and to achieve a strong interference spectrum. Once an acceptable interference pattern was achieved, the fibre pieces were permanently glued to the glass slide.

Three sensor types were fabricated for evaluation purposes using the above manufacturing process. All three sensor types utilised corning single mode (SMF28) lead-in and lead-out fibres that have a numerical aperture (NA) of 0.13, mode field diameter (MFD) of 9.3 μm (± 0.5 μm), and a core diameter of 8.2 μm. Specifications of the sensor types (A, B and C) are provided below:

3.1. Sensor Type – A

This sensor type utilizes a 4.00 mm (± 0.15 mm) long NKT Photonics HC-PCF (HC-PCF 1550) fiber as the sensing element. The HC-PCF fiber has a numerical aperture (NA) of 0.2, mode field diameter (MFD) of 9.00 μm (± 1 μm) and core diameter of 10.00 μm. This sensing fiber element also has cladding air holes of diameter 3.10 μm and a cladding pitch of 3.80 μm. The fiber has a narrow wavelength transmission window of 1490-to-1680 nm that supports several guided modes in this band.

3.2. Sensor Type – B

This sensor type utilizes a 4.00 mm (± 0.15 mm) long Thorlabs HC19-PCF fiber as the sensing element. The HC-PCF fiber has a numerical aperture (NA) of 0.13, mode field diameter (MFD) of 13.00 μm (± 2 μm) and core diameter of 20.00 μm. This sensing fiber element also has cladding air holes of diameter 3.10 μm and a cladding pitch of 3.80 μm. The fiber has a narrow wavelength transmission window of 1490-to-1680 nm, that supports several guided modes in this band.

3.3. Sensor Type – C

This sensor type utilizes a 4.00 mm (± 0.15 mm) long NKT Photonics Low Loss single-mode fibres (LMA-10) with a solid core as the sensing element. This PCF fiber has a numerical aperture (NA) of 0.11, mode field diameter (MFD) of 10.50 μm (± 1 μm) and core diameter of 10.00 μm. Important features of this fibre type are low transmission loss, single-mode light transmission at all wavelengths, and a wavelength independent MFD.

In the experimental tests described in Sections 5.1 and 5.2, the lead-in and lead-out gap distances are fixed at 1.00 mm. In Section 5.3, the lead-in and lead-out gap distances are varied between 0.00 and 5.00 mm in 50-μm increments for each gap.

Fig. 3a and b illustrate a normalized transmission spectrum and fringe spacing of Sensor Type-A (gaps of 1.00 mm) immersed in a test

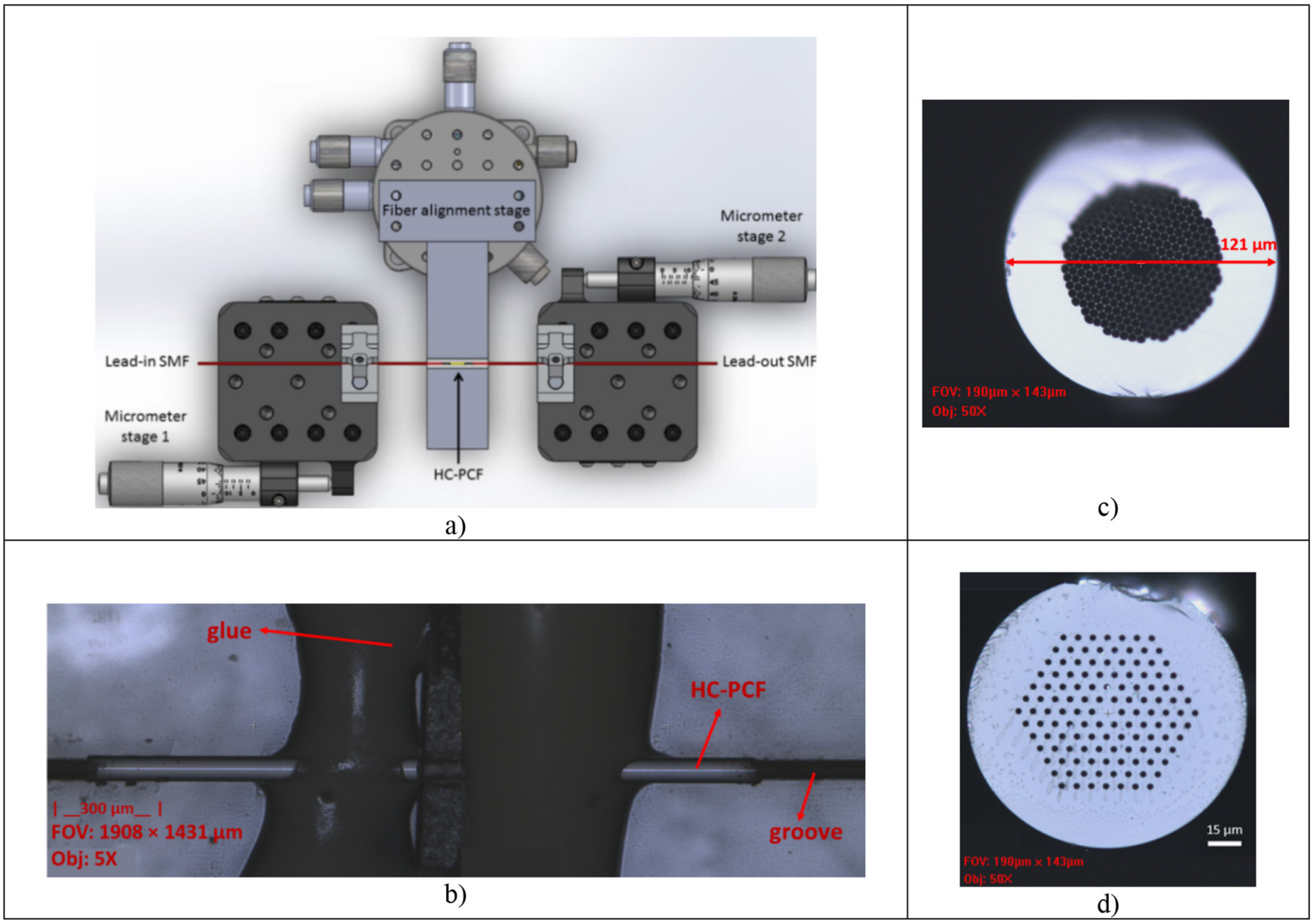

Fig. 2. (a) Top view of the fabrication setup using a fibre alignment stage and two linear-translation micro-stages for control of gap distances, (b) microscopic image of a sensing element glued to the microscope glass, (c) image of 10 µm HC-PCF fibre (Sensor Type-A), (d) image of solid-core PCF fiber (Sensor Type-C).

chamber containing Nitrogen at atmospheric pressure. Each valley measured at the sensor's output (Fig. 3a) results from interference between the signal arms in the MZI at that wavelength. Sensor-Type A has fringe spacing of 1.22 nm. Sensor-Types B and C have fringe spacing of 1.31 and 1.20, respectively.

4. Experimental procedure

The first set of experiments conducted on the sensor types (A, B, and C) investigated the variation in the refractive index of the sensing element and gas combination. The schematic diagram of Fig. 4 shows the overall arrangement of the sensor evaluation system, including the spectrum analyzer, input fiber circulator, the sensor fiber, and the gas

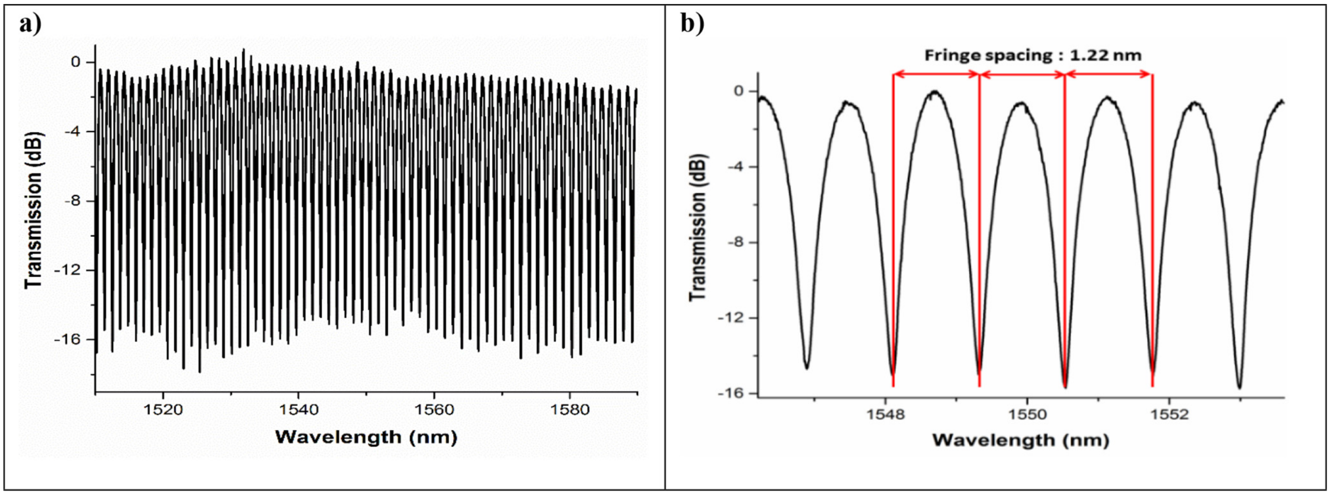

Fig. 3. (a) Normalized transmission spectrum of Sensor Type-A with length of 4 mm and gaps of 1 mm immersed in Nitrogen at room temperature and atmospheric pressure, (b) Fringe spacing measured at the lead-out side of Sensor Type-A.

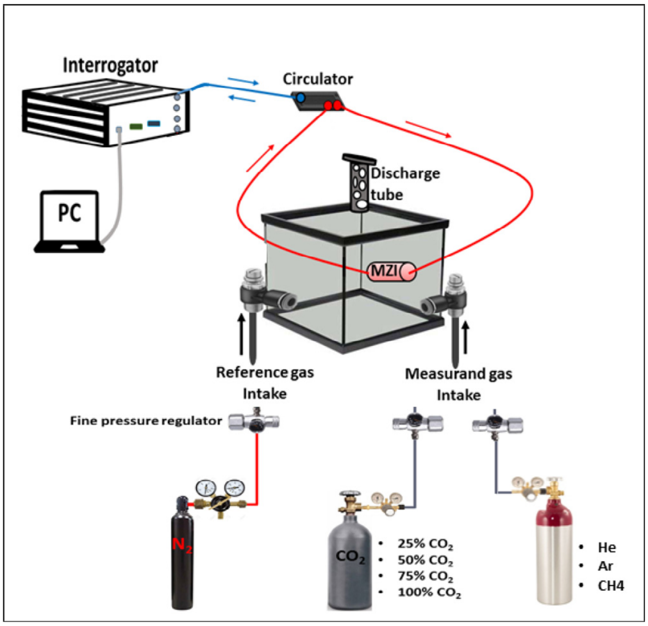

Fig. 4. Schematic of the experimental setup: tests were carried out at room temperature and atmospheric pressure.

intake valves connected to the test chamber. The test chamber has dimensions of 14.5 cm × 11.2 cm × 4.4 cm, and allows two gas sources to be connected via intake valves: (i) Nitrogen (N_2) gas which is used as a reference, and (ii) test (measurand) gases consisting of 25%, 50%, 75%, and 100% concentrations of CO_2, helium, argon, and methane. In addition, pressure regulators were connected to the gas lines to ensure a constant injection pressure of 15 psi was maintained through the testing process. A discharge tube with a bubbler was used to sustain the pressure inside the test chamber. A Micron Optics interrogator (SM125), with a resolution of 1 pm, was used to record and evaluate changes in the transmission spectrum. In addition, a Fibre Bragg Grating (FBG) sensor, with a sensitivity of 10 pm/°C, was used to monitor and record the temperature fluctuations inside the chamber. The Micron Optics' Enlight software was used to record and analyze the spectral shifts of the three sensor types and the FBG.

The experiments started with injecting N_2 into the test chamber until an even gas diffusion into all the PCF and HC-PCF's air holes was achieved. The measurand gases were then individually injected into the chamber and sensor responses were recorded using the Micron optics interrogator. Cyclic tests were carried out to examine the repeatability of RI measurements using the proposed sensors. Subsequently, important sensing performance parameters were studied, including RI sensitivity and the sensor response and recovery times. The spectral response of each sensor type is a function of the gas species injected into the chamber, the pressure and temperature. Therefore, as part of the sensor characterization process, the FBG was placed in-line with the sensors and the temperature fluctuations within the chamber were simultaneously recorded in order to compensate for temperature effects. Reliable operation and repeatable sensing capability are essential in any sensing application, especially in gas sensing. Therefore, the sensors were characterized several times and at different wavelengths, using a constant time interval (7 min) for each test gas at the different concentrations. Each sensor's output signal was interrogated for the gas under evaluations and the sensors showed a consistent trend in wavelength shifts (Fig. 5).

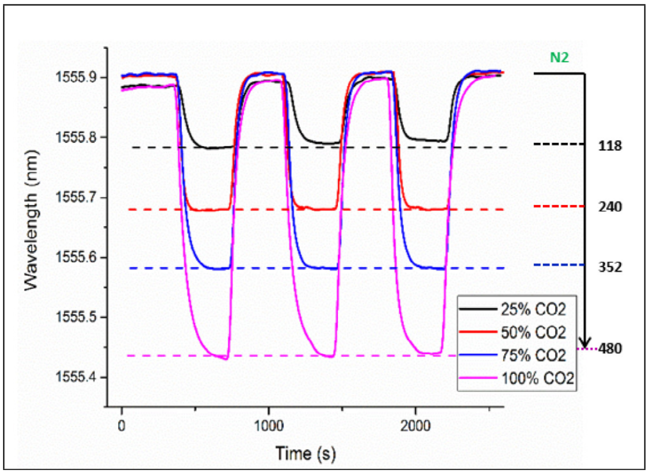

Fig. 5. The spectral response of Sensor Type-A to different concentrations of CO_2 for 3 cycles, and a gap length of 1.00.

5. Results and discussion

5.1. Refractive index measurement of the test gas in the sensing element

Fig. 5 illustrates the response of Sensor Type-A to carbon dioxide for three experimental cycles and with a fixed lead-in and lead-out distance of 1.00 mm. The sensor was individually interrogated to analyze its spectral response to CO_2 and a complete test cycle consisted of measuring the spectral response for the reference gas (99.99% pure nitrogen); followed by an injection and measurement of CO_2 (for 7 min); and finally, an injection of nitrogen back into the chamber to purge the CO_2. In comparison with the position of the spectrum resulting from measurement of the reference gas, Sensor Type-A showed wavelength spectrum wavelength shifts of 118 pm, 240 pm, 352 pm, and 480 pm when immersed in 25%, 50%, 75%, and 100% concentrations of CO_2. The transmission spectrum for the sensor underwent a blue shift in response to the presence of CO_2. The RI of CO_2 is higher than the RI of nitrogen, which resulted in the blue shift of the interference fringes. In the transmission interference fringe, spectral shifts of three different valleys, at different wavelengths, were used to calculate wavelength shifts and measurement errors.

Fig. 6 illustrates the response of Sensor Type-A to argon, helium, and methane for three experimental cycles. The sensor's wavelength response depended on the gas species injected into the chamber. In comparison with the position of the spectrum resulting from measurement of the reference gas, Sensor Type-A showed spectrum shifts of

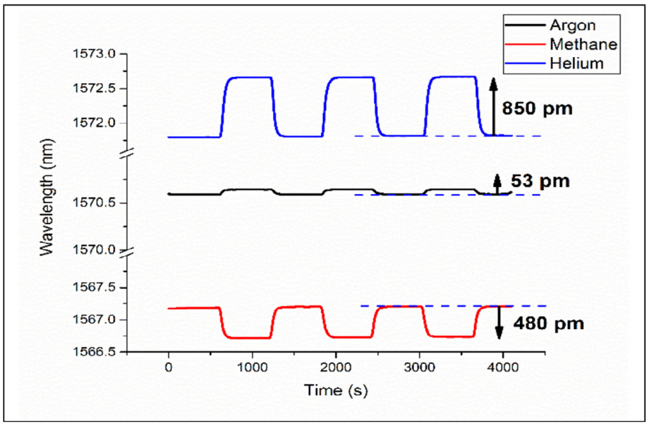

Fig. 6. The spectral response of Sensor Type-A to 100% concentrations of Argon (99.99% pure), Helium (99% pure), and Methane for 3 cycles.

Table 1
Total wavelength shifts of MZI sensors for helium, methane, argon, and different concentrations of CO_2.

Sensor Type	**Lead-in/out distance**	Spectral shift (pm) in helium	Spectral shift (pm) in methane	Spectral shift (pm) in 25% CO_2	Spectral shift (pm) in 50% CO_2	Spectral shift (pm) in 75% CO_2	Spectral shift (pm) in 100% CO_2	Spectral shift (pm) in argon	**RI sensitivity (nm/RIU)**
A (10 μm)	**~ 1 mm**	850	470 (negative)	118 (negative)	240 (negative)	352 (negative)	480 (negative)	53	**3210**
B (20 μm)	**~ 1 mm**	670	430 (negative)	100 (negative)	210 (negative)	315 (negative)	432 (negative)	40	**2660**
C (PCF)	**~ 1 mm**	510	363 (negative)	95 (negative)	195 (negative)	263 (negative)	377 (negative)	30	**2140**

850 pm (± 6 pm), 53 pm (± 3 pm), and 470 pm (± 5 pm) when immersed in He, Ar, and CH_4, respectively. The transmission spectrum for each sensor test underwent red shifts in response to Ar and He, and blue shifts in response to CH_4. This finding can be explained as spectral response to a change in RI. Because the RIs of helium and argon are considerably lower than the RI of nitrogen, the interference fringe showed a red shift.

Table 1 summarizes the wavelength shifts of the entire family of sensor types (A, B, and C) to the measurand gases, as described above. The RI sensitivity achieved in this work is high, compared with the performance of alternative approaches described in the research literature. For example, a sensitivity of 1233 nm/RIU was reported for a HC-PCF MZI sensor [58], 1053 nm/RIU was reported for a cavity based Fabry-Perot [59], and 1546 nm/RIU was achieved for a Fabry-Perot sensor based on a hollow silica tube [60]. Sensor Type-A shows the highest wavelength shifts. In contrast, Sensor Type-C shows the lowest shifts when immersed in the measurand gases. The RI sensitivity of each MZI sensor in the RI range of 1.0000347–1.000449 is recorded in Table 1. The highest sensitivity of 3210 (nm/RIU) for Sensor Type-A and lowest sensitivity of 2140 (nm/RIU) for Sensor Type-C in the given RI range was achieved.

5.2. Performance parameters of MZI sensors

Response and recovery times are defined as the time the sensors required to reach 90% of the final value of the total wavelength shift. Fig. 7a is an example that shows response and recovery times for detection of methane with Sensor-A. Results indicate that Sensor-B shows the fastest response/recovery time, while Sensor-C had the slowest response/recovery time. This result can be attributed to the hollow-core structures of sensors A and B, compared to the solid-core structure of Sensor-C. The proposed HC-PCF MZI sensor has, nonetheless, the potential for advancing current capacity for low-percentage gas detection, environmental monitoring, and quantitatively analyzing changes in pure gases. Since the performance of the tested MZI sensors were evaluated at atmospheric pressure and room temperature, they can be used for detection of any pure gas with high precision. The RI of a target gas ($RI_{target\ gas}$) can be expressed by the following equation:

$$RI_{targetgas} = RI_{N_2} - \Delta RI = RI_{N_2} - \Delta\lambda/(RIsensitivity) \tag{5}$$

where$RI_{N_2}$is the RI of the reference "N_2" gas, ΔRI is the relative difference in RI of a target and "N_2" gas. The ΔRI can be calculated using the wavelength shift ($\Delta\lambda$) of the interference fringe factoring in the sensitivity of the sensor. The $\Delta\lambda$ can be obtained by tracking a transmission valley of the interference fringes. Fig. 7b illustrates the sensitivity graph of Sensor-A to ambient RI change for the given RI range.

In order to analyze the number and power distribution of the modes participating in the modal interference process, the transmission spectrum of each sensor was Fourier transformed to obtain its corresponding spatial frequency, described as [61]:

$$v = \frac{\Delta n_{eff}.\ D}{\lambda^2} \tag{6}$$

Δn_{eff} is the effective RI difference between core and cladding of the sensing element, and D is the distance between the two ends of the SMFs. To be able to examine the characteristics of measured interference in Fourier domain, the wavelength spectra of each MZI sensor in the presence of various gases were Fourier transformed. Fig. 8a shows the spatial frequency response of Sensor-A in the presence of a pure gas, such as nitrogen, helium, methane, and carbon dioxide. The dominant peak corresponds to the interference between one higher-order mode and the fundamental mode. A characteristic of this figure's data is that the magnitude of the spatial frequency for the dominant peak is constant in the presence of measurand gases with different RI, but the amplitude of the peaks varies [62]. The amplitude of each peak corresponds to the amount of power carried by that mode. For example,

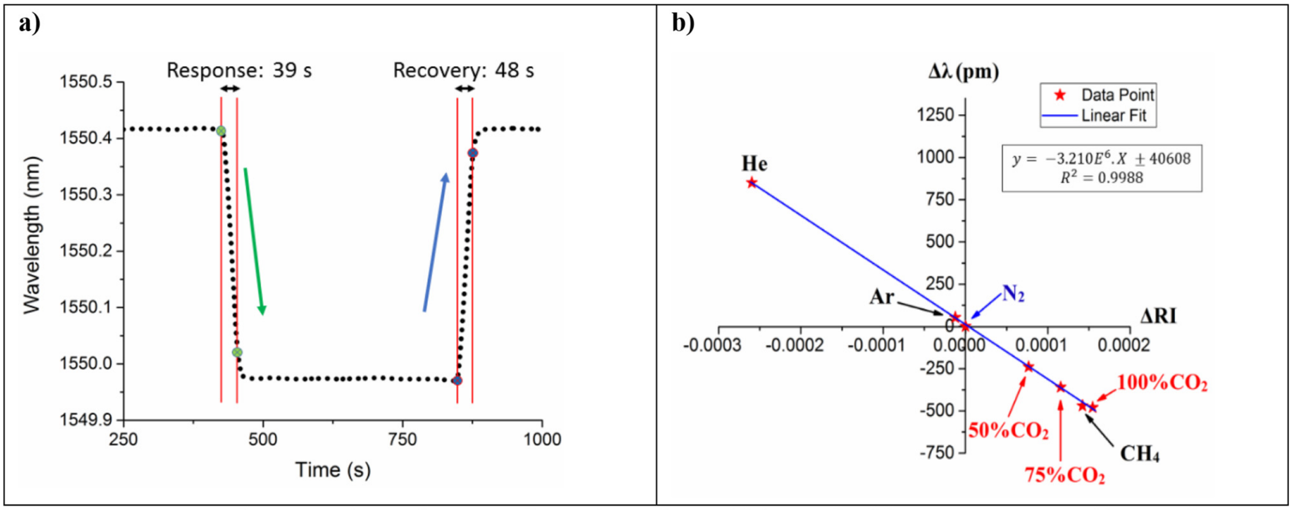

Fig. 7. (a) Response and recovery times of Sensor-A for methane, (b) sensitivity graph of the same sensor to ambient RI change.

for Sensor-A, power of dominant mode has the minimum amplitude of 2.11 for helium, and the maximum amplitude of 2.58 for nitrogen. Sensor-C (Fig. 8b) carried the dominant mode with the minimum amplitude of 1.91 for nitrogen, and the maximum amplitude of 2.22 for helium. This method is another approach to characterize and distinguish the presence of different gases. In order to clarify the performance of each MZI, in the next section of this report, effect of structure of the sensing element on the carrying power of each mode is explained.

5.3. *Spatial frequency analysis of effect of fibre structure and gap length on number and power distribution of modes for MZI gas sensor*

A second set of experiments were performed to analyze the effect of gap distance, as well as structure of the sensing element on the modal interference of the proposed MZI gas sensors. The lead-in and lead-out SMFs were not glued to the microscope slide so that it was possible to change gap distance on both sides of the sensing element. Linear translation stages were used to alter the gap lengths on each side of the sensing element; each gap was increased from 0 to 5.00 mm in 50-µm increments (D in Eq. (6) varied from 4 mm to 14 mm in 100 µm increments in the mentioned formula of spatial frequency). While maintaining equal gap distance on both sides of the sensing element, 100 transmission spectrums were collected for each of three types of MZI configuration: (i) a 10 µm core HC-PCF sensing element, (ii) a 20 µm core HC-PCF sensing element, and (iii) a solid core PCF as the sensing element. The spectrums were processed through a Fourier Transform in order to obtain spatial frequency graphs of each sensing element type and examine the number and power distribution of the modes. Different peaks in the spatial frequency graph correspond to the interference between fundamental mode and different higher order modes.

5.3.1. *Spatial frequency analysis of MZI sensors with solid core PCF*

For the MZI with solid-core PCF, spatial frequency analysis revealed that the power is mainly carried by one mode (core-cladding 1) in the spatial frequency spectrum for gap distances ranging from 0 to 3.75 mm. For gap lengths higher than 3.75 mm, the amplitude of the dominant mode decreases dramatically. Fig. 9a shows the spatial frequency graph for a PCF-MZI sensor with $D = 6.5$ mm, which contains a dominant mode at 9.5×10^{-4} (1/nm). Highest amount of power

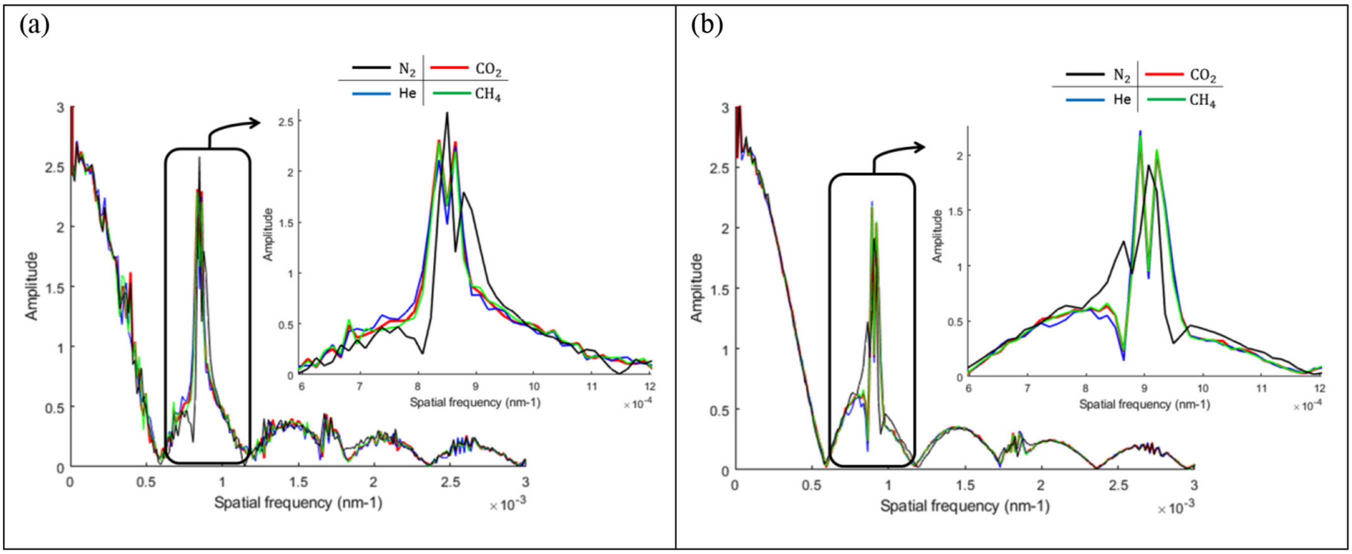

Fig. 8. (a) Effect of gas RI on spatial frequencies for Sensor-A; The dominant mode has an amplitude of 2.11, 2.28, 2.31 and 2.58 for pure helium, carbon dioxide, methane and nitrogen respectively. (b) Similar effect for Sensor-C; the dominant mode has an amplitude of 1.91, 2.16, 2.17 and 2.2 for pure helium, carbon dioxide, methane and nitrogen respectively.

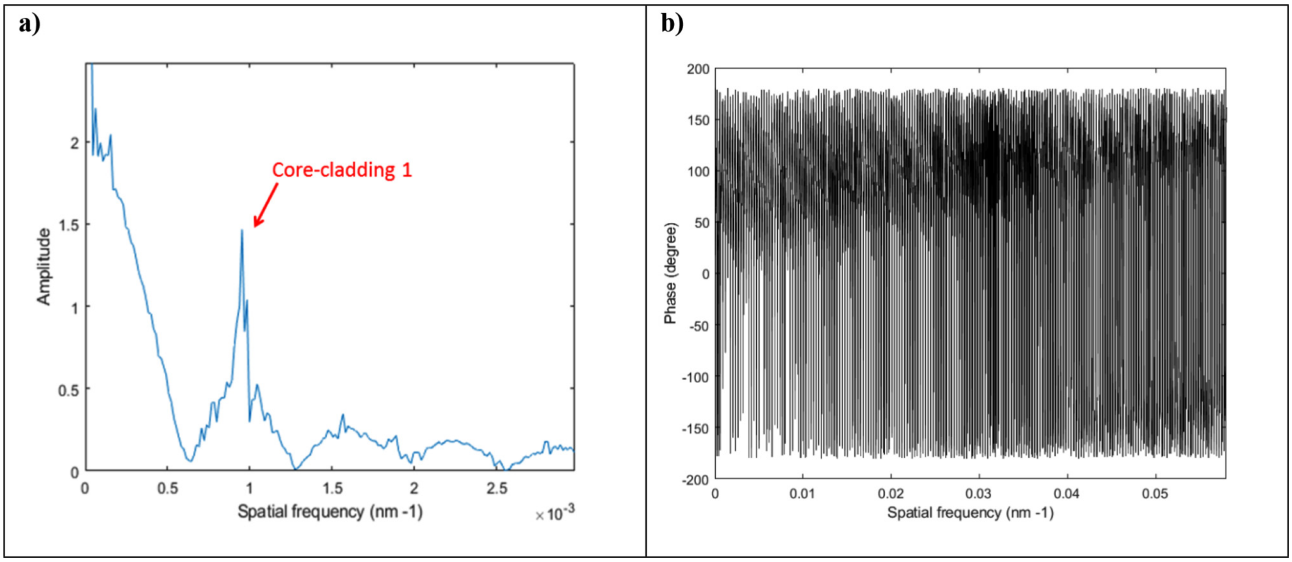

Fig. 9. (a) Spatial frequency graph for a solid-core PCF MZI with PCF length of 4 mm and D of 6.5 mm; here, power is mainly carried by one mode. (b) The phase diagram of the same sensor; the dominant mode has a phase shift of 148 degrees.

carried by the dominant mode was recorded at $D = 11.3$ mm with normalized FFT value of 3.56, which is higher than FFT values for HC-PCF sensors. Phase shift information produced by the MZI sensors can also be extracted from the spatial frequency graph. Fig. 9b illustrates the phase diagram of the MZI presented in Fig. 9a, and reveals that the dominant mode has a phase shift of 148 degrees.

5.3.2. Spatial frequency analysis of MZI sensors with 10 μm core HC-PCF

It was shown that the power is mainly distributed between two dominant modes in the spatial frequency spectrum, as gap distances increased. This behaviour confirms that higher order modes would gradually leak off the sensing fibre and experience transmission losses, and fewer peaks would turn up in the spatial frequency graph due to a weakening interference effect. Fig. 10a shows the spatial frequency graph for the MZI with 10 μm HC-PCF and gaps of 1.5 mm on sides ($D = 7$ mm). The same device is made up of a strong cladding mode with a spatial frequency of 5×10^{-4} (1/nm) and normalized FFT value of 3.14, which is named core-cladding 1. Besides this dominant cladding mode, the sensor also contains a relatively weaker cladding mode (core-cladding 2) with a spatial frequency of 1.1×10^{-3} (1/nm) and a normalized FFT value of 0.99. It was found that for sensors with gaps from 0 to 1.65 mm core-cladding 1 is the dominant cladding mode, while for higher gaps core-cladding 2 became the dominant mode. The highest power transmission was found in an MZI with gaps of 1.35 mm, and the amplitude of spatial frequencies decreased intensely for gaps higher than 4.5 mm. Fig. 10b was plotted by tracking dominant modes of the MZI with respect to D. It shows how the magnitudes of spatial frequencies increase by increasing length of gaps. As the spatial frequencies are obtained by equation (6) and transmission spectrums of MZIs, instability of light source as well as inaccuracy in the distance between two ends of SMFs can impose errors on spatial frequency values. For example, ± 0.15 mm tolerance in a 4 mm stub of sensing element can lead to errors from 1% (for D = 14 mm) to 3.75% (for D = 4 mm) on spatial frequency values. Errors associated with gap lengths can be eliminated by using automated fiber positioning systems. Besides, by equal splitting of fundamental core mode of the lead-in fiber into core and cladding modes of the HC-PCF, transmission fringe can be improved.

The results of measured phase shifts of the MZI can be compared with the calculated phase shifts (see equation (2)) for the same sensor. The core-cladding 1 mode of the MZI sensor travels through the core and the first layer of air-holes in the cladding (those closest to the hollow-core). The calculated phase shift of the dominant mode in this MZI is 168 degrees, while the measured phase shift of the dominant

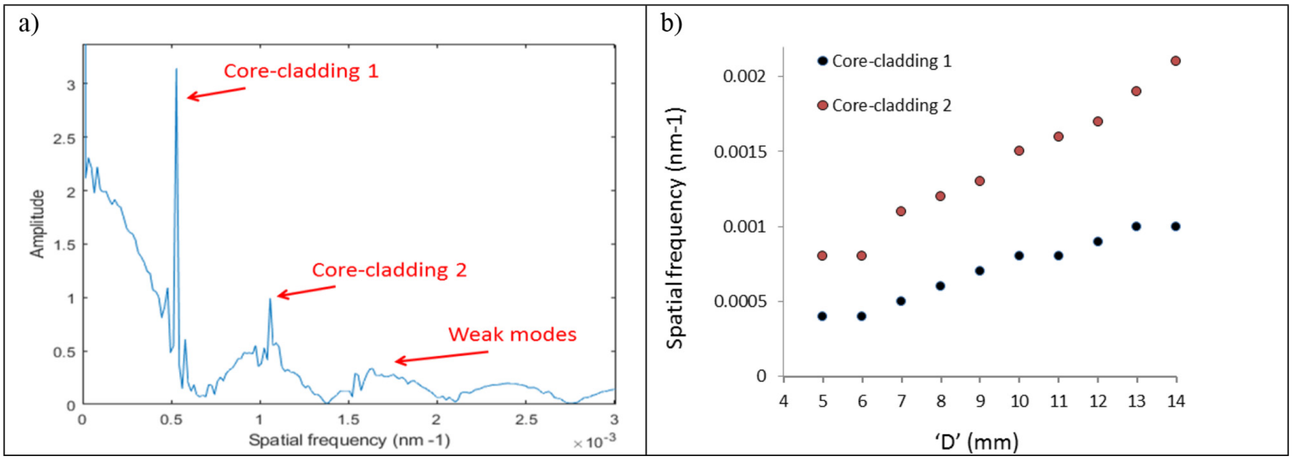

Fig. 10. (a) Spatial frequency graph for a 10 μm HC-PCF MZI with HC-PCF length of 4 mm and D of 7 mm, (b) tracking dominant modes of the sensor with respect to D, where power is mainly distributed between two dominant modes.

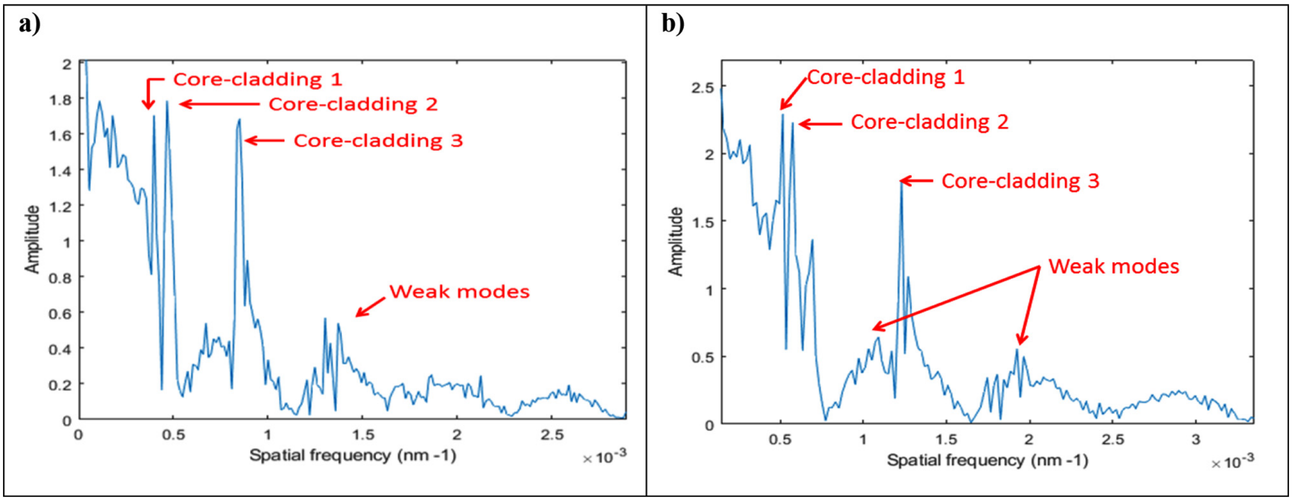

Fig. 11. Spatial frequency graph for a 20 μm HC-PCF MZI with HC-PCF length of 4 mm and (a) D of 6 mm, (b) D of 8.4 mm. Power is mainly distributed between three dominant modes.

mode is 172 degrees. A difference of about 2.2% exists between the measured and calculated phase shifts. The dominant mode in the 10 μm HC-PCF MZI with highest power transmission has a phase shift of 160 degrees.

5.3.3. Spatial frequency analysis of MZI sensors with 20 μm core HC-PCF

Fig. 11a and b show spatial frequencies for the MZI with 4 mm of 20 μm HC-PCF as the sensing element, with gaps of 1 mm and 2.2 mm on both sides. 100 data points were analysed for this sensor, with D varying from 4 mm to 14 mm in 100 μm steps. As shown in Fig. 11, several modes are involved in the modal interference and power is mainly distributed in three dominant modes in the spatial frequency spectrum, as gap distances increased for the MZI with 20 μm HC-PCF. Some higher-order modes would leak the sensing fiber, similar to processes observed in the MZI with 10 μm HC-PCF, but results indicate that stronger interferences as well as a higher number of modes can be carried by 20 μm HC-PCF sensors. Fig. 11a shows three strong core-cladding modes with spatial frequencies of 3.9×10^{-4} (1/nm), 4.6×10^{-4} (1/nm), and 8.5×10^{-4} (1/nm) followed by a weaker mode at 1.3×10^{-3} (1/nm).

Experiment results indicate that for gap distances from 0 to 0.75 mm on each side, core-cladding 1 was the dominant mode. The highest amount of power carried by this mode was recorded at $D = 4.8$ mm (with gaps of 0.4 mm) and at 2.9×10^{-4} (1/nm). For gap distances higher than 2.5 mm on each side, core-cladding 3 became the dominant mode and the highest amount of power carried by this mode was observed for $D = 10$ mm (with gaps of 3 mm) and at 1.4×10^{-3} (1/nm). Phase shift information of this MZI reveals that the dominant mode has a phase shift of 166 degrees.

The amplitude of spatial frequencies decreases continuously when gaps are set at 3.5 mm and higher. By tracking normalized FFT values of dominant modes, it was concluded that for gap distances ranging from 0.8 mm to 3.15 mm all three dominant modes carry high amounts of power. This observation contrasts to the results obtained by experimenting with a 10 μm HC-PCF MZI. So, higher power transmission occurs with a 20 μm HC-PCF than through the other tested sensing element configurations.

6. Conclusion

A compact PCF-based interferometric sensor structure is proposed and has been experimentally demonstrated for sensitive detection of gases. Several sensors were fabricated and characterized using 3 types of photonic crystal fibre as the sensing element. The resulting fibre sensors were able to measure the RI of a gas-filled cavity and each showed excellent sensitivity to helium, methane, argon, and various concentrations of carbon dioxide. The highest RI sensitivity of 3210 nm/RIU was demonstrated in the RI range of 1.0000347–1.000449 for a sensor with 4 mm length of 10 μm HC-PCF. This shows an improvement over results obtained through previous laboratory research and experimental design. Results of the present project indicate that the 20 μm HC-PCF MZI sensor shows the fastest response/recovery time, while solid-core PCF-MZI shows the slowest response/recovery time. The effects of gap distances on the number and amplitude distribution of the sensors' modes were examined. Spatial frequency analysis revealed that power is mainly carried by two dominant modes in the 10 μm MZI, three dominant modes in the 20 μm MZI, and one mode in the solid-core PCF. Highest amount of power transmission was recorded for an MZI with solid core PCF. It was concluded that by using 20 μm HC-PCF as sensing element of the MZI, stronger interference occurs, and higher number of modes can be carried by this fiber. In addition, power transmission and phase shift of dominant modes were studied for MZIs with different sensing elements. This sensor type is a suitable choice for low-percentage detection of gases as well as environmental monitoring.

CRediT authorship contribution statement

Kaveh Nazeri: Proposed and performed experiments, Formal analysis, Validation, Writing - original draft. **Colin Bradley:** Supervision, Resources, Writing - review & editing.

Declaration of Competing Interest

The authors declare that they have no known competing financial interests or personal relationships that could have appeared to influence the work reported in this paper.

Acknowledgments

The Natural Sciences and Engineering Research Council (NSERC) of Canada supported this work.

References

[1] B. Lee, Review of the present status of optical fiber sensors, Opt. Fiber Technol. 9 (2) (2003) 57–79.
[2] K.T.V.a.T.S. Grattan, Fiber optic sensor technology; an overview, Sens. Actuat. A 82 (2000) 40–61.

[3] K. Fidanboylu, H.S. Efendioğlu, Fiber optic sensors and their applications, in: 5th International Advanced Technologies Symposium (IATS'09), 2009.
[4] J. Villatoro, D. Monzón-Hernández, Low-cost optical fiber refractive-index sensor based on core diameter mismatch, J. Lightwave Technol. 24 (3) (2006) 1409.
[5] M.P. Buric, et al., Enhanced spontaneous Raman scattering and gas composition analysis using a photonic crystal fiber, Appl. Opt. 47 (23) (2008) 4255–4261.
[6] X. Yang, et al., Multiplexed gas sensing based on Raman spectroscopy in photonic crystal fiber, in: IEEE Photonics Conference 2012, 2012.
[7] G. Stewart, et al., Design of a fibre optic multi-point sensor for gas detection, Sens. Actuat. B 51 (1) (1998) 227–232.
[8] G. Stewart, F.A. Muhammad, B. Culshaw, Sensitivity improvement for evanescent-wave gas sensors, Sens. Actuat. B: Chem. 11 (1) (1993) 521–524.
[9] X. He, G.A. Rechnitz, Linear response function for fluorescence-based fiber-optic CO2 sensors, Anal. Chem. 67 (13) (1995) 2264–2268.
[10] A. Abdelghani, et al., Surface plasmon resonance fibre-optic sensor for gas detection, Sens. Actuat. B 39 (1) (1997) 407–410.
[11] A.C. Elosua, F.J. Arregui, I.D. Villar, C. Ruiz-Zamarreño, J.M. Corres, C. Bariain, J. Goicoechea, M. Hernaez, P.J. Rivero, A.B. Socorro, et al., Micro and nanostructured materials for the development of optical fibre, Sensors 17 (2017) 2312.
[12] C. Elosua, I.R. Matias, C. Bariain, F.J. Arregui, Volatile organic compound optical fiber sensors: a review, Sensors 6 (2006) 1440–1465.
[13] Y.-P. Miao, W. Jin, F. Yang, Y.-C. Lin, Y.-Z. Tan, L.H. Hoi, Advances in optical fiber photothermal interferometry for gas detection, Wuli Xuebao/Acta Phys. Sin. (2017) 66.
[14] J. Lin, Recent development and applications of optical and fiber-optic pH sensors, TrAC Trends Anal. Chem. 19 (2000).
[15] A. Rivero, P.J. Goicoechea, F.J. Arregui, Optical fiber sensors based on polymeric sensitive coatings, Polymers 10 (3) (2018) 280.
[16] A. Fasano, G. Woyessa, P. Stajanca, C. Markos, A. Stefani, K. Nielsen, H.K. Rasmussen, K. Krebber, O. Bang, Fabrication and characterization of polycarbonate microstructured polymer optical fibers for high temperature-resistant fiber Bragg Grating strain sensors, Opt. Mater. Express 6 (2) (2016) 649.
[17] A.G. Leal-Junior, A. Frizera, M. José Pontes, Sensitive zone parameters and curvature radius evaluation for polymer optical fiber curvature sensors, Opt. Laser Technol. 100 (2018) 272–281.
[18] G. Woyessa, K. Nielsen, A. Stefani, C. Markos, O. Bang, Temperature insensitive hysteresis free highly sensitive polymer optical fiber Bragg grating humidity sensor, Opt. Express 24 (2) (2016) 1206–1213.
[19] G. Woyessa, J.K.M. Pedersen, A. Fasano, K. Nielsen, C. Markos, H.K. Rasmussen, O. Bang, Zeonex-PMMA microstructured polymer optical FBGs for simultaneous humidity and temperature sensing, Opt. Lett. 42 (6) (2017) 1161–1164.
[20] C.A.F. Marques, R. Min, A. Leal Junior, P. Antunes, A. Fasano, G. Woyessa, K. Nielsen, H.K. Rasmussen, B. Ortega, O. Bang, Fast and stable gratings inscription in POFs made of different materials with pulsed 248 nm KrF laser, Opt. Express 26 (2018) 2013–2022.
[21] Rui Min, Beatriz Ortega, Carlos Marques, Fabrication of tunable chirped mPOF Bragg gratings using a uniform phase mask, Opt. Express 26 (2018) 4411–4420.
[22] G. Arnaldo, Antreas Theodosiou Leal-Junior, Carlos Marques, Maria José Pontes, Kyriacos Kalli, Anselmo Frizera, Compensation method for temperature cross-sensitivity in transverse force applications with FBG sensors in POFs, J. Lightwave Technol. 36 (2018) 3660–3665.
[23] A. Leal-Junior, A. Theodosiou, C. Díaz, et al., Polymer optical fiber bragg gratings in CYTOP fibers for angle measurement with dynamic compensation, Polymers (Basel) 10 (6) (2018) 674.
[24] C.A.F. Marques, A. Pospori, G. Demirci, et al., Fast bragg grating inscription in PMMA polymer optical fibres: impact of thermal pre-treatment of preforms, Sensors (Basel) 17 (4) (2017) 891.
[25] Carlos Marques, Leal Junior, Rui Arnaldo, Min, et al., Advances on polymer optical fiber gratings using a KrF pulsed laser system operating at 248 nm, Fibers 6 (2018) 13.
[26] R. Min, C. Marques, K. Nielsen, O. Bang, B. Ortega, Fast inscription of long period gratings in microstructured polymer optical fibers, IEEE Sens. J. 18 (2018) 1919–1923.
[27] S. Saharudin, K.M. Isha, Z. Mahmud, S.H. Herman, U.M. Noor, Performance evaluation of optical fiber sensor using different oxygen sensitive nano-materials, in: Proceedings of the 2013 IEEE 4th International Conference on Photonics (ICP), Melaka, Malaysia, 2013, pp. 309–312.
[28] M. Zolkapli, S. Saharudin, S.H. Herman, W.F.H. Abdullah, The influence of sol-gel coated length and withdrawal rate on plastic optical fiber core towards oxygen gas sensing sensitivity, J. Teknol. 78 (2016) 87–91.
[29] Fatima Domingues, Camilo Rodriguez, Joana Martins, et al., Cost-effective optical fiber pressure sensor based on intrinsic Fabry-Perot interferometric micro-cavities, Opt. Fiber Technol. 42 (2018) 56–62.
[30] R. Wang, X. Qiao, Hybrid optical fiber Fabry-Perot interferometer for simultaneous measurement of gas refractive index and temperature, Appl. Opt. 53 (2014) 7724–7728.
[31] H. Sun, J. Zhang, Q. Rong, D. Feng, Y. Du, X. Zhang, et al., A hybrid fiber interferometer for simultaneous refractive index and temperature measurements based on Fabry–Perot/ Michelson interference, IEEE Sens. J. 13 (5) (2013) 2039–2044.
[32] P. Jia, G. Fang, T. Liang, Y. Hong, Q. Tan, X. Chen, et al., Temperature-compensated fiber-optic Fabry-Perot interferometric gas refractive-index sensor based on hollow silica tube for high-temperature application, Sens. Actuat. B 244 (2017) 226–232.
[33] Qiang Liu, Liang Xin, Wu Zhaoxia, Refractive index sensor of a photonic crystal fiber Sagnac interferometer based on variable polarization states, Appl. Phys Express 12 (6) (2019).
[34] L. Li, L. Xia, Z. Xie, D. Liu, All-fiber Mach-Zehnder interferometers for sensing applications, Opt. Express 20 (2012) 11109–11120.
[35] H.Y. Choi, M.J. Kim, B.H. Lee, All-fiber Mach-Zehnder type interferometers formed in photonic crystal fiber, Opt. Express 15 (9) (2007) 5711–5720.
[36] X. Chen, et al., Temperature insensitive bending sensor based on in-line Mach-Zehnder interferometer, Photonic Sensors 4 (3) (2013) 193–197.
[37] L.M. Hu, et al., Photonic crystal fiber strain sensor based on modified Mach-Zehnder interferometer, IEEE Photonics J. 4 (1) (2012) 114–118.
[38] J. Fu, et al., In-fiber M-Z interferometer based on cascaded long period gratings in embedded-core fiber, IEEE Photonics Technol. Lett. 29 (21) (2017) 1876–1879.
[39] Lili Mao, Ping Lu, Zefeng Lao, Deming Liu, Jiangshan Zhang, Highly sensitive curvature sensor based on single-mode fiber using core-offset splicing, Opt. Laser Technol. 57 (2014) 39–43, https://doi.org/10.1016/j.optlastec.2013.09.036.
[40] Q. Wang, et al., Comparative analyses of Bi-tapered fiber mach-zehnder interferometer for refractive index sensing, IEEE Trans. Instrum. Meas. 66 (9) (2017) 2483–2489.
[41] F. Ahmed, et al., Bragg grating embedded in Mach-Zehnder interferometer for refractive index and temperature sensing, IEEE Photonics Technol. Lett. 28 (18) (2016) 1968–1971.
[42] M. Deng, et al., Highly sensitive temperature sensor based on an ultra-compact Mach-Zehnder interferometer with side-opened channels, Opt. Lett. 42 (18) (2017) 3549–3552.
[43] J.-N. Wang, J.-L. Tang, Photonic crystal Fiber Mach-Zehnder interferometer for refractive index sensing, Sensors 12 (3) (2012).
[44] S. Wu, et al., Mode-filtered light methane gas sensor based on cryptophane A, Anal. Chim. Acta 633 (2) (2009) 238–243.
[45] Jianchun Yang, Lang Zhou, Jing Huang, Chuanyi Tao, Xueming Li, Weimin Chen, Sensitivity enhancing of transition mode long-period fiber grating as methane sensor using high refractive index polycarbonate/cryptophane A overlay deposition, Sens. Actuat. B 207 (2015) 477–480, https://doi.org/10.1016/j.snb.2014.10.013.
[46] S. Liu, et al., Liquid-filled simplified hollow-core photonic crystal fiber, Opt. Laser Technol. 64 (2014) 140–144.
[47] C. Tao, et al., Optical fiber sensing element based on luminescence quenching of silica nanowires modified with cryptophane-A for the detection of methane, Sens. Actuat. B 156 (2) (2011) 553–558.
[48] R.F. Cregan, et al., Single-mode photonic band gap guidance of light in air, Science 285 (5433) (1999) 1537.
[49] E.J.H. Bo Dong, Core-offset hollow core photonic bandgap fiber based intermodal interferometer for strain and temperature measurement, Opt. Soc. Am. 50 (2011) 3011–3014.
[50] W. Jin, H.L. Ho, Y.C. Cao, J. Ju, L.F. Qi, Gas detection with micro- and nano-engineered optical fibers, Opt. Fiber Technol. 19 (6) (2013) 741–759, https://doi.org/10.1016/j.yofte.2013.08.004.
[51] D.N. Wang, Micro-engineered optical fiber sensors fabricated by femtosecond laser micromachining, in: Imaging and Applied Optics Technical Papers, Optical Society of America, Monterey, California, 2012.
[52] L. Xuefeng, et al., Fabrication of photonic bandgap fiber gas cell using focused ion beam cutting, Japanese J. Appl. Phys. 48 (6S) (2009) 06FK05.
[53] K. Nazeri, V. Ahsani, F. Ahmed, H. Joe, M. Jun, C. Bradley, Experimental comparison of the effect of the structure on MZI fiber gas sensor performance, in: 2019 IEEE Pacific Rim Conference on Communications, Computers and Signal Processing (PACRIM), Victoria, BC, Canada, 2019, pp. 1–6.
[54] G.Z. Xiao, et al., Monitoring changes in the refractive index of gases by means of a fiber optic Fabry-Perot interferometer sensor, Sens. Actuat. A 118 (2) (2005) 177–182.
[55] F. Benabid, P.J. Roberts, Linear and nonlinear optical properties of hollow core photonic crystal fiber, J. Mod. Opt. 58 (2) (2011) 87–124.
[56] Z. Zhi-guo, et al., Gas sensing properties of index-guided PCF with air-core, Opt. Laser Technol. 40 (1) (2008) 167–174.
[57] W. Wang, M. Guo Wei, Y. Zhao, Optimization of cascaded fiber tapered Mach-Zehnder interferometer and refractive index sensing technology, Sens. Actuat. B Chem. 222 (2016).
[58] N.L.P. Andrews, R. Ross, D. Munzke, C. van Hoorn, A. Brzezinski, J. A. Barnes, et al., In-fiber Mach-Zehnder interferometer for gas refractive index measurements based on a hollow-core photonic crystal fiber, Opt. Express 24 (2016): 14086–14099, 2016/06/27.
[59] M.S. Ferreira, L. Coelho, K. Schuster, J. Kobelke, J.L. Santos, O. Frazão, Fabry–Perot cavity based on a diaphragm-free hollow-core silica tube, Opt. Lett. 36 (2011): 4029–4031, 2011/10/15.
[60] P. Jia, G. Fang, T. Liang, Y. Hong, Q. Tan, X. Chen, et al., Temperature-compensated fiber-optic Fabry–Perot interferometric gas refractive-index sensor based on hollow silica tube for high-temperature application, Sens. Actuat. B: Chem. 244 (2017): 226–232, 2017/06/01/.
[61] H. Zhang, S. Gao, Y. Luo, Z. Chen, Ultrasensitive Mach-Zehnder interferometric temperature sensor based on liquid-filled D-shaped fiber cavity, Sensors 18 (2018): 1239. 10.3390/s18041239.
[62] Hai-wei, et al., Fourier analysis applied on MZI transmission spectrum for refractive index measurement, Photonics Technol. Lett. IEEE 27 (2015) 658–660.